



This is a repository copy of *An image-based kinematic model of the tibiotalar and subtalar joints and its application to gait analysis in children with Juvenile Idiopathic Arthritis.*

White Rose Research Online URL for this paper:
<http://eprints.whiterose.ac.uk/141524/>

Version: Accepted Version

Article:

Montefiori, E., Modenese, L., Di Marco, R. et al. (10 more authors) (2019) An image-based kinematic model of the tibiotalar and subtalar joints and its application to gait analysis in children with Juvenile Idiopathic Arthritis. *Journal of Biomechanics*. ISSN 0021-9290

<https://doi.org/10.1016/j.jbiomech.2018.12.041>

Article available under the terms of the CC-BY-NC-ND licence
(<https://creativecommons.org/licenses/by-nc-nd/4.0/>).

Reuse

This article is distributed under the terms of the Creative Commons Attribution-NonCommercial-NoDerivs (CC BY-NC-ND) licence. This licence only allows you to download this work and share it with others as long as you credit the authors, but you can't change the article in any way or use it commercially. More information and the full terms of the licence here: <https://creativecommons.org/licenses/>

Takedown

If you consider content in White Rose Research Online to be in breach of UK law, please notify us by emailing eprints@whiterose.ac.uk including the URL of the record and the reason for the withdrawal request.



eprints@whiterose.ac.uk
<https://eprints.whiterose.ac.uk/>

30
31
32
33
34
35
36
37
38
39
40
41
42
43
44
45
46
47
48
49
50
51

Abstract

In vivo estimates of tibiotalar and the subtalar joint kinematics can unveil unique information about gait biomechanics, especially in the presence of musculoskeletal disorders affecting the foot and ankle complex. Previous literature investigated the ankle kinematics on ex vivo data sets, but little has been reported for natural walking, and even less for pathological and juvenile populations. This paper proposes an MRI-based morphological fitting methodology for the personalised definition of the tibiotalar and the subtalar joint axes during gait, and investigated its application to characterise the ankle kinematics in twenty patients affected by Juvenile Idiopathic Arthritis (JIA). The estimated joint axes were in line with in vivo and ex vivo literature data and joint kinematics variation subsequent to inter-operator variability was in the order of 1°. The model allowed to investigate, for the first time in patients with JIA, the functional response to joint impairment. The joint kinematics highlighted changes over time that were consistent with changes in the patient's clinical pattern and notably varied from patient to patient. The heterogeneous and patient-specific nature of the effects of JIA was confirmed by the absence of a correlation between a semi-quantitative MRI-based impairment score and a variety of investigated joint kinematics indexes. In conclusion, this study showed the feasibility of using MRI and morphological fitting to identify the tibiotalar and subtalar joint axes in a non-invasive patient-specific manner. The proposed methodology represents an innovative and reliable approach to the analysis of the ankle joint kinematics in pathological juvenile populations.

Key words: Biomechanics, Ankle joint axis, Musculoskeletal modelling, Gait analysis, Patient-specific modelling

52 **Introduction**

53 Functional anatomy literature describes the ankle joint as a very complex structure allowing for multiple
54 movements due to the combination of various mechanically coupled joints, including the tibiotalar (i.e.
55 between tibia and talus) and subtalar (i.e. between talus and calcaneus) joints (Hicks et al., 1953; Siegler et
56 al., 1988; Dettwyler et al., 2004). The biomechanical behaviour of the ankle during locomotion and its
57 relationship with the anatomy have been investigated since the beginning of the last century (Fick, 1911;
58 Manter, 1941; Barnett and Napier, 1952; Isman and Inman, 1969; Inman, 1976) and many authors have
59 also estimated the kinematics of the tibiotalar and subtalar joints ex vivo (Hicks et al., 1953; Rasmussen and
60 Tovborg-Jensen, 1982; van Langelaan, 1983; Siegler et al., 1988). The possibility of estimating the
61 kinematics of the ankle's intrinsic joints from in vivo data is of interest when investigating musculoskeletal
62 diseases. Nonetheless, a comprehensive understanding of the joint's intrinsic movement during walking is
63 still lacking. This is because measuring the motion associated to foot inversion/eversion is not trivial and
64 most literature has focused on the quantification of articular range of motion (ROM) for the various joint's
65 degrees of freedom (DOFs) under controlled conditions (Lundberg et al., 1989; Mattingly et al., 2006;
66 Lewis et al., 2009).

67 In vivo tracking of the relative movement of the talus relative to the calcaneus using skin markers and a
68 standard gait analysis technique is complicated by the small size of these bones and the absence of visible
69 superficial landmarks (Scott et al., 1991; Di Marco et al., 2016). Few studies have investigated the
70 kinematics of the intrinsic joints of the ankle during walking and running (Arndt et al., 2004 and 2006)
71 using intracortical bone pins, and compared the results to those from using superficial markers (Westblad
72 et al., 2002). These studies clearly showed a description of plantar/dorsiflexion is possible with traditional
73 gait analysis methods, however, estimates of inversion/eversion movement are still far from being accurate.
74 Intracortical pin-based studies partially overcome this lack of accuracy but, due to the invasiveness of the
75 technique, the number of participants is usually limited to few healthy volunteers, whose natural gait pattern
76 can be altered by the possible pain and discomfort related to the implant. Both in vivo and ex vivo studies

77 reported high intra-subject and inter-subject variability in the subtalar joint kinematics with ROM up to 60°
78 (Roaas and Anderson, 1982; Sepic et al., 1986; Lundberg, 1989).

79 The functional complexity of the subtalar joint led to a number of different modelling approaches, from the
80 attempt to capture its mobility through multi-segmental foot models where the subtalar articulation was
81 interpreted as a motion between hind-foot and fore-foot (Prinold et al., 2016; Saraswat et al., 2010), to a
82 more anatomical representation as a universal or hinge joint (Delp et al., 1990; Malaquias et al., 2017). The
83 hinge-like schematisation also applies to the tibiotalar joint and this approach is currently used within
84 widely adopted musculoskeletal models (Delp et al., 1990). When simultaneously modelling both joints as
85 hinges (Dul and Johnson, 1985), a reasonable simplification is made with respect to their real functional
86 role (Siegler et al., 1988), according to which the tibiotalar and subtalar joints describe
87 the plantar/dorsiflexion and inversion/eversion motions, respectively. This latter motion, despite its
88 simplified appearance, is justified because the predominant motion occurs about a single axis of rotation
89 (Scott and Winter, 1991). However, this DOF has been reported to be less accurately described with current
90 musculoskeletal modelling approaches, mainly due to the difficulties in identifying the joint functional axis
91 in vivo (Van den Bogert et al., 1994; Dettwyler et al., 2004; Parr et al., 2012). A high variability within-
92 and between-subjects has been observed in the modelled joint axes, which is also related to the specific
93 locomotion task (Leitch et al., 2010). In the presence of musculoskeletal disorders, the adoption of image-
94 based patient-specific modelling approaches has been previously proposed (Prinold et al., 2016; Hannah et
95 al., 2017) and proved to increase anatomical modelling accuracy (Correa and Pandy 2011; Durkin et al.,
96 2006; Scheys et al., 2009). The use of this technique accounts for patients' anatomical features and
97 peculiarities, crucial when impairments and gait limitations affect the subjects. In this study, we propose an
98 image-based modelling procedure to define the tibiotalar and subtalar joints axes, avoiding operator-
99 dependent steps and related variability issues (Prinold et al., 2016; Hannah et al., 2017). Once compared
100 against literature, the procedure will be used as part of a patient-specific musculoskeletal modelling
101 approach to investigate the gait ankle kinematics in children with Juvenile Idiopathic Arthritis (JIA), a

102 paediatric group of diseases of unknown aetiology characterised by joint inflammation potentially leading
103 to cartilage damage. Altered gait patterns and physical disabilities (Ravelli and Martini, 2007) are possible
104 outcomes in JIA. This longitudinal study will prove whether our modelling approach is capable of detecting
105 clinical changes observed in the tibiotalar and the subtalar joint functions and quantify for the first time the
106 relationship between these changes and the underlying joint impairments.

107 **Methods**

108 **2.1 Subjects and data acquisition**

109 Twenty participants (5 males, 15 females, age: 11.6 ± 3.1 years, mass: 47.6 ± 18.2 kg, height: 148 ± 17 cm, 11
110 new onsets) affected by Juvenile Idiopathic Arthritis (JIA) of various sub-types (oligoarticular onset JIA,
111 polyarticular JIA, psoriatic arthritis, and undifferentiated arthritis) (Ravelli and Martini, 2007) were
112 recruited among those referred to two different children's hospitals (Istituto Giannina Gaslini, Genoa (Lab
113 1), and "Bambino Gesù" Children's Hospital, Rome (Lab 2)). The study was conducted following
114 Helsinki's declaration on human rights and was approved by the ethical committee of both hospitals.
115 Written informed consent was obtained by patients' parents.

116 Medical resonance images (MRI) and gait analysis data were collected at three time-points (6 months apart)
117 to follow the disease progression. The imaging performed at month 0 (M0) and month 12 (M12) included
118 a foot and ankle regional MRI (multi-slice multi-echo 3D Gradient Echo (mFFE) with water-only selection
119 (WATS) with 0.5 mm in-plane resolution and 1 mm slice thickness). The month 6 (M6) imaging included
120 a full lower limb MRI (3D T1-weighted fat-suppression sequence (e-THRIVE) with 1mm in-plane
121 resolution and 1mm slice thickness). The core set of basic sequences and definitions suggested by the
122 Outcome Measure in Rheumatology (OMERACT) MRI Working Group (Ostergaard et al., 2003; Nusman
123 et al., 2016) was used to provide an MRI-based evaluation of the joints (Table I). A weighted, average index
124 (I_{MRI}) was used to quantify the overall level of impairment of the foot and ankle region.

Table I - MRI scoring.

Index	MRI sequence	Scale	Sites
Bone erosion	T1-weighted fat-saturated	Range 0-10 % of eroded articular surface (<i>Ostergaard et al., 2003</i>) 0 = no erosion; 1 = 1–10%; 2 = 11–20%; 3 = 21–30%; 4 = 31–40%; 5 = 41–50%; 6 = 51–60%; 7 = 61–70%; 8 = 61–80%; 9 = 81–90%; 10 = 91–100%	Distal tibial epiphysis Distal fibula epiphysis Tarsal bones Metatarsal bases
Cartilage damage	WATS	Range 0-3 % of damaged cartilage surface 0 = no damage; 1 = 1–33%; 2 = 34–66%; 3 = 67–100%; 4 = extensive damage causing ankyloses	Tibiotalar Between distal talus and calcaneus, Talonavicular Calcaneocuboid Cuneonavicular Between cuneiforms and I, II and III metatarsal bones Between cuboid and IV and V metatarsal bones
Synovitis	T1-weighted fat-saturated	Range 0-3 Degree of synovial enhancement and synovial thickness (<i>Ostergaard et al., 2003; Malattia et al., 2011</i>) 0 = normal; 1 = mild; 2 = moderate; 3 = severe	Tibio-peroneo-talar Subtalar Talonavicular Calcaneocuboid I-V tarsometatarsal Cuneonavicular
Tenosynovitis	T1-weighted fat-saturated with enhancement	Range 0-3 Degree of peritendinous effusion or synovial proliferation 0 = normal; 1 = mild (< 2 mm); 2 = moderate (2 -5 mm); 3 = severe (> 5 mm)	Anterior tibial Extensor digitorum longus Extensor hallucis longus Posterior tibial Flexor digitorum longus Flexor hallucis longus Peroneal tendons

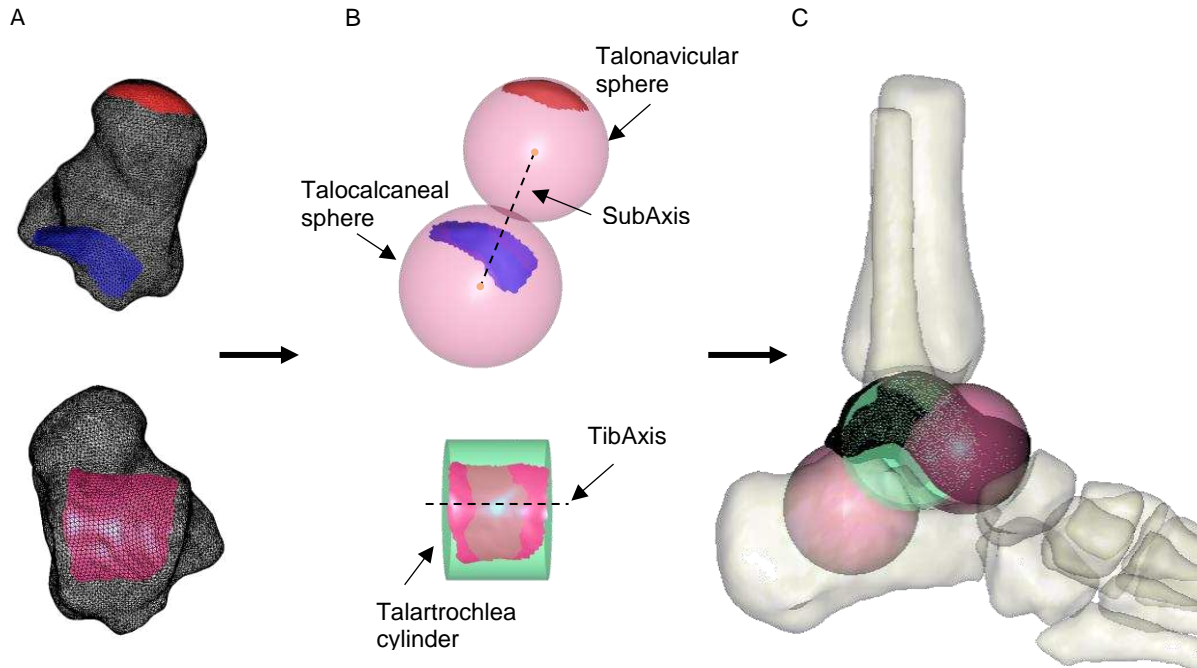
126

127 Gait analysis was based on stereophotogrammetry and data were collected using a 6-camera system (BTS,
128 Smart DX, 100Hz) with two force plates (Kistler, 1kHz) in Lab 1, and an 8-camera system (Vicon, MX,
129 200Hz) and two force plates (AMTI, OR6, 1kHz) in Lab 2. Five walking trials at self-selected speed were
130 performed and a minimum of three trials were used for the analysis. The marker set included forty-four
131 markers from the Vicon Plug in gait protocol (Vicon Motion System) and the modified Oxford Foot Model
132 (mOFM) protocol (Stebbins et al., 2006). A subset of MRI-visible markers (twenty-eight in the lower limb
133 MRI and six in the regional MRI scans) was retained during the imaging acquisition for data registration.

134 Despite being collected in different centres and with different equipment, the raw-data underwent the same
135 pre-processing in terms of labelling, gap-filling (spline algorithm built in Vicon Nexus 1.8.5 (Woltring et
136 al., 1986)), and smoothing (4th-order Butterworth filter, 6Hz cut-off (Barlett et al., 2007)).

137 **2.2 Anatomical model**

138 A statistical shape modelling approach (Steger et al., 2012) was used to segment the lower limb bones from
139 the MRI and subject-specific anatomical models were produced using specialised software (NMSBuilder,
140 Valente et al., 2017). For each patient, two bilateral three-segment anatomical models were built using the
141 M0 and M12 datasets, resulting in 80 foot models. Twelve of these were excluded due to incompleteness
142 of the experimental dataset, resulting in a final dataset of 68 feet. The joints' reference frames, namely
143 tibiotalar joint (between tibia and talus) and subtalar (between talus and foot) were defined according to the
144 ISB conventions (Baker et al., 2003) and the joint axes were identified through morphological fitting of
145 articular surfaces (Figure 1A-C). The subtalar joint axis (SubAxis) was defined as the axis connecting the
146 centres of the spheres fitted to the anterior (Talonavicular sphere) and to the posterior-inferior
147 (Talocalcaneal sphere) facets of the talus respectively (Figure 1B). This was similar to that proposed by
148 Parr et al., 2012, who, however, used the anterior-inferior portion of the talus surface to define the
149 Talonavicular sphere. To define the tibiotalar joint axis (TibAxis), a cylinder was fitted to the entire trochlea
150 (Talarochlea cylinder) as a simplification of the approach proposed by Siegler et al., 2014 (Modenese et
151 al., 2018). The fitting was implemented in Meshlab (Cignoni et al., 2008) by identifying the articular
152 surfaces from the segmented geometries and minimising the least squares distance between the identified
153 surface and the corresponding best fitting analytical shape (Least Squares Geometric Elements library,
154 Matlab). The distal tibia (segmented from the M0/12 MRI) was afterwards registered to the entire tibia (M6
155 dataset) using the Iterative Closest Point algorithm in Meshlab to obtain a full lower limb model. A
156 comprehensive description of the modelling procedure is available as supplementary material in Modenese
157 et al. (2018). The data and models presented in this paper are available on Figshare (doi:
158 <https://doi.org/10.15131/shef.data.5863443.v1>).



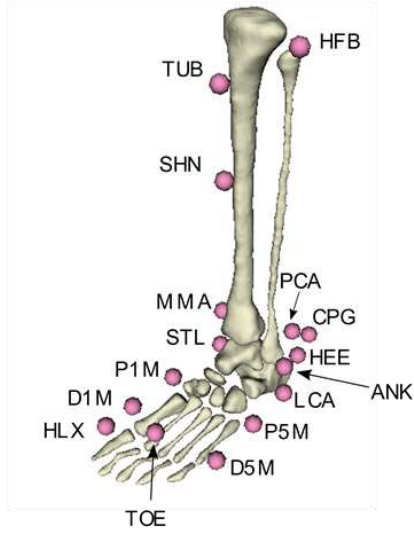
159

160 **Figure 1 - (A) Plantar (top) and dorsal (bottom) views of the right talus (black wireframe) with**
 161 **highlighted articular regions: anterior facet (red), posterior-inferior facet (blue), trochlea (fuchsia). (B)**
 162 **Fitting of analytical shapes to the selected articular regions: two spheres (light pink) identify the axis of**
 163 **the subtalar joint (SubAxis) as the axis connecting the centres of the spheres and a cylinder (light green)**
 164 **identifies the axis of the tibiotalar joint (TibAxis) as the cylinder axis. (C) Example of the fitted**
 165 **geometries integrated within the ankle anatomical model.**

166

167 2.3 Joint kinematics

168 The OpenSim's (Delp et al., 2007) Inverse Kinematics (IK) tool was run to estimate the tibiotalar and
 169 subtalar joint angles starting from a set of sixteen skin markers (five on the tibia, eleven on the foot, Figure
 170 2), eight were also virtually palpated on the medical images. The difference between the virtual and
 171 experimental markers estimated by the IK tool was less than 1cm on average over all the time-steps, as
 172 suggested in the OpenSim best practice recommendations (Hicks et al., 2015).



Label	Description	Markers	
		MRI	Stereo
HFB	Head of the fibula	Yes	Yes
SHN	Anterior aspect of shin	Yes	Yes
TUB	Tibial tuberosity	-	Yes
MMA	Medial malleolus	Yes	Yes
ANK	Lateral malleolus	Yes	Yes
PCA	Posterior medial aspect of heel	-	Yes
STL	Sustentaculum tali	-	Yes
LCA	Lateral calcaneus	-	Yes
CPG	Wand marker on posterior calcaneus aligned with transverse orientation	-	Yes
HEE	Posterior distal aspect of heel	-	Yes
P1M	Lateral aspect of 1 st metatarsal base	-	Yes
P5M	Lateral aspect of 5 th metatarsal base	-	Yes
TOE	Between 2 nd and 3 rd metatarsal heads	Yes	Yes
D1M	Lateral aspect of 1 st metatarsal head	Yes	Yes
D5M	Lateral aspect of 5 th metatarsal head	Yes	Yes
HLX	Medial side of the proximal hallux	Yes	Yes

173

174 **Figure 2 - Experimental markers used in the imaging (MRI) and stereo-photogrammetric (Stereo)**
 175 **measurements.**

176 **2.4 Model evaluation**

177 **Sensitivity to operator-dependent input**

178 The bone segmentations from three randomly chosen patients were used to investigate the effect of
 179 operator-dependent variability in the definition of TibAxis and SubAxis. Three operators repeated the
 180 morphological fitting three times and the coordinates of the Talartrochlea cylinder, Talocalcaneal sphere
 181 and Talonavicular sphere centres were used for the comparison. A 3D quantification of their variability
 182 (SD_{3d}) was calculated from the standard deviation of the point coordinates (sd_x, sd_y, sd_z) as:

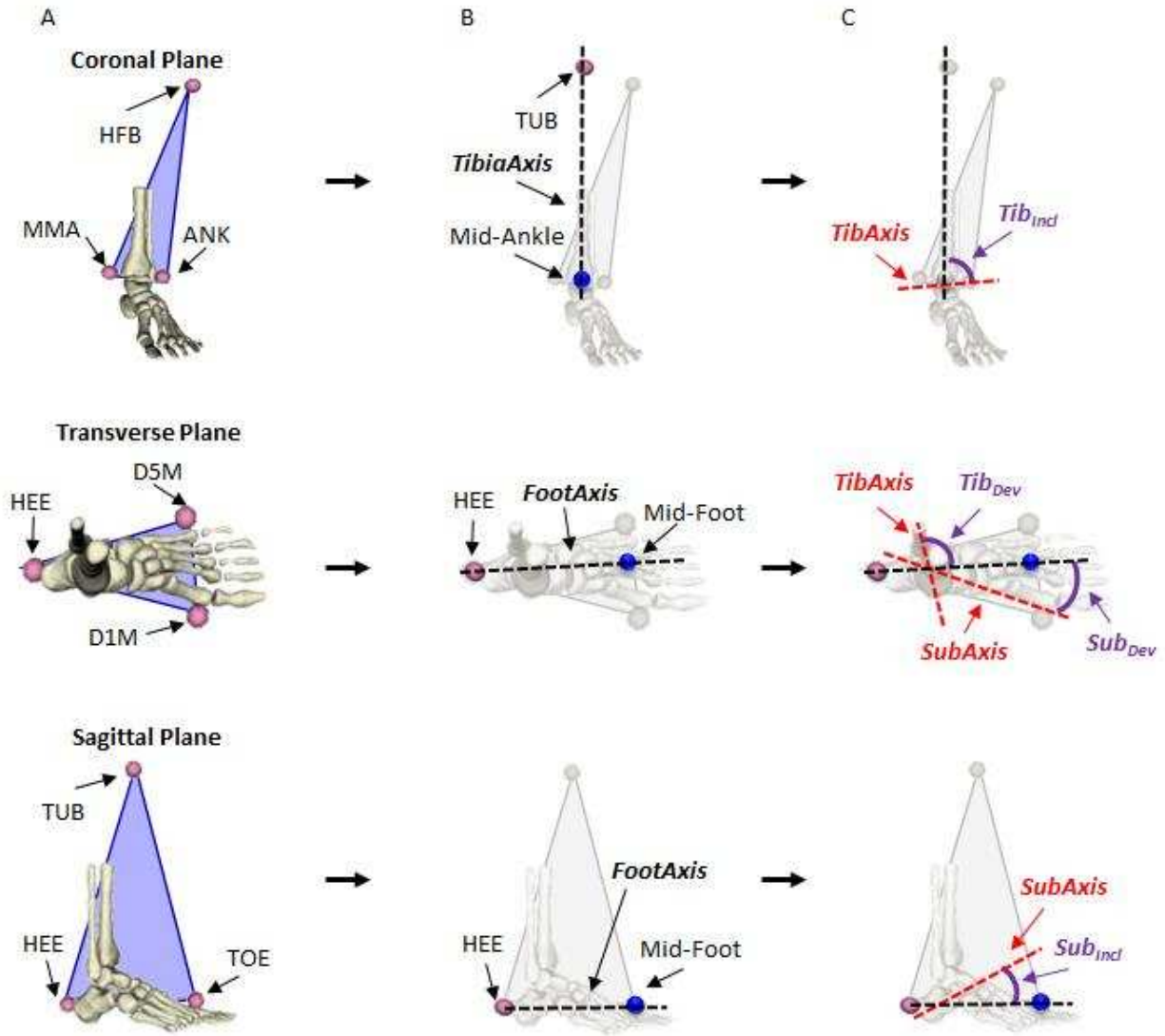
183
$$SD_{3d} = \sqrt{sd_x^2 + sd_y^2 + sd_z^2}$$

184 For the foot that led to the worst-case scenario (higher inter-operator SD_{3d}), a second level of analysis was
 185 conducted to quantify the propagation of this error on the joint kinematics. The nine models built by the
 186 three operators were then used to estimate the tibiotalar and subtalar joint kinematics using data from one

187 randomly selected gait trial from the same patient. The maximum value of the mean and standard deviation
188 calculated over the nine repetitions for each point of the gait cycle was then used to quantify the maximum
189 expected error.

190 **Consistency with literature data**

191 Among the 68 available models, 38 were selected (19 per side, preferentially from M12) to conduct the
192 following analysis. A standing trial collected during the gait analysis session was used to identify the pose
193 of each subject and the resulting neutral position of the foot. The transverse, sagittal, and coronal anatomical
194 planes, the midline of the foot (FootAxis) and the long axis of tibia (TibiaAxis) were identified using the
195 standing trial markers (Figure 3A-B). These allowed quantifying the tibiotalar inclination (Tib_{Incl}) and
196 deviation (Tib_{Dev}), and the subtalar inclination (Sub_{Incl}) and deviation (Sub_{Dev}) as shown by the angles in
197 Figure 3C. Tib_{Incl} , Tib_{Dev} , Sub_{Incl} and Sub_{Dev} were compared to literature data from ex vivo cadaveric
198 specimens (Isman and Inman., 1969; Inman, 1976) and from healthy adults (Van den Bogert et al., 1994).
199 The estimations of TibAxis and SubAxis at M0 and M12 were also compared. All 26 models for which the
200 3D anatomy was available at both time-points (52 models) were used for a between-session comparison.
201 For this analysis, the angle between the two joint axes (InterAxis) was preferred over the measures of Tib_{Incl} ,
202 Tib_{Dev} , Sub_{Incl} , and Sub_{Dev} to avoid the effect of experimental markers repositioning (between the two
203 sessions) on these angles. Mean and maximum between-session variations were quantified, and a paired-
204 two-sided Wilcoxon signed-rank test ($\alpha=0.05$) was performed under the null hypothesis showed that no
205 statistical difference existed between the two repeated measures. This was intended as a repeatability
206 assessment of the proposed method, assuming in the investigated age range, and within 12 months, neither
207 disease progression (Ravelli and Martini, 2007) nor growth (Evans, 2010) would cause changes in the joint
208 morphology.



209
210

211 **Figure 3 - (A) Identification of anatomical planes (blue triangles) as defined using the virtual markers (pink) corresponding to the experimental markers listed in Figure 2. (B) Definition of the anatomical axes (midline of the foot = FootAxis, long axis of the tibia = TibiaAxis, black dashed lines) by calculating average points (blue markers) between virtual marker pairs (Mid-Foot = midpoint between D1M and**
 212 **(pink) corresponding to the experimental markers listed in Figure 2. (B) Definition of the anatomical axes (midline of the foot = FootAxis, long axis of the tibia = TibiaAxis, black dashed lines) by calculating**
 213 **average points (blue markers) between virtual marker pairs (Mid-Foot = midpoint between D1M and**
 214 **D5M; Mid-Ankle = midpoint between ANK and MMA). (C) Quantification of the inclination (TibIncl)**
 215 **and deviation (TibDev) of tibiotalar joint and inclination (SubIncl) and deviation (SubDev) of subtalar**
 216 **joint as the angles (purple arches) between the anatomical axes and the joint axes (red dashed lines) as**
 217 **defined through morphological fitting (Figure 1).**
 218

219 **Effect of clinical impairment on joint kinematics**

220 The models from 13 subjects (3 males, 10 females, age: 11.0 ± 3.1 years, mass: 44.5 ± 16.9 kg, height: 143
 221 ± 13 cm, 8 new onsets), for whom both clinical and biomechanical information was available, were used to

222 test the link between changes in the kinematics and impairment of the ankle as measured from the MRI.
223 The I_{MRI} scores were used to classify the disability level of each ankle and identify better and worse time-
224 points. They were then placed into “low-involvement” and “high-involvement” groups accordingly. The
225 joint kinematics of the two groups were then compared using a non-parametric 1D two-tailed paired t-test
226 ($\alpha=0.05$) (Nichols and Holmes, 2002) based on Statistical Parametric Mapping (SPM) in MATLAB (v9.1,
227 R2016b, Mathworks, USA), using the SPM1D package (Pataky et al., 2012). This was chosen since the
228 data were not normally distributed. The following kinematic parameters were also calculated to investigate
229 the correlation with the I_{MRI} : area under the curves of the tibiotalar and subtalar joint angles, maximum
230 plantarflexion (PF) and dorsiflexion (DF) angles, maximum inversion (Inv) and eversion (Ev) angles, and
231 joint ROM. Furthermore, the asymmetry between the left and right foot kinematics was quantified using
232 the Root Mean Square Deviation (RMSD) and Mean Absolute Variability (MAV) (Di Marco et al., 2018),
233 as well as the between-side difference of ROM and standard deviations (SD). RMSD, MAV, ROM and SD
234 were measured at the two time-points and compared using a two-sided Wilcoxon signed-rank test ($\alpha=0.05$).
235 The absolute difference (ΔI_{MRI}) between left and right I_{MRI} was also calculated and a correlation analysis
236 was used to assess whether an asymmetry in the clinical score, namely higher ΔI_{MRI} , corresponded to higher
237 values of the kinematic parameters.

238 **Results**

239 **Sensitivity to operator-dependent input**

240 SD_{3d} of Talonavicular sphere and *Talocalcaneal sphere's* centres are reported in Table II, as well as the
241 resulting maximum angular variability of the TibAxis and SubAxis, whose maximum value (9.6°) was found
242 for the inclination of SubAxis in patient P3. For this patient, the propagation of inter-operator variability on
243 the articular kinematics introduced a maximum standard deviation of 0.6° and 1.3° for the tibiotalar and
244 subtalar joints respectively, both occurring at 63% of the gait cycle.

245

Table II – Inter-operator standard deviation (SD) of fitted surfaces centres and axes.

	<i>Talartrochlea center</i>	<i>Talonavicular center</i>	<i>Talocalcaneal center</i>	<i>TibAxis</i>	<i>SubAxis</i>
Patients	<i>SD</i>_{3d} [mm]	<i>SD</i>_{3d} [mm]	<i>SD</i>_{3d} [mm]	SD [°]	SD [°]
P1	0.4	0.4	1.4	0.6	1.7
P2	0.5	0.8	1.5	0.8	1.3
P3	0.8	2.1	5.1	2.0	5.6

246

247 **Consistency with literature data**

248 The residual error of the fitting algorithm (average (\pm SD) across the 52 models) was equal to 0.16 (\pm 0.05)
 249 mm, 0.48 (\pm 0.21) mm, and 0.28 (\pm 0.11) mm for the Talonavicular, Talocalcaneal, and Talartrochlea
 250 surfaces, respectively. The average (\pm SD) values of the measured foot angles (Tib_{Incl} , Tib_{Dev} , Sub_{Incl} , and
 251 Sub_{Dev}) (Table III) were found to be in line with the corresponding ex vivo (Isman and Inman., 1969; Inman,
 252 1976) and in vivo (Van den Bogert et al., 1994) measurements available in the literature. The average
 253 absolute difference between the M0 and M12 measures of InterAxes was $2.2^\circ \pm 2.1^\circ$, which was not
 254 statistically significant (Wilcoxon test $p=0.648$).

255

Table III - Inclination and deviation of tibiotalar and subtalar joint axes and comparison with published literature datasets (n = numebr of subjects).

256

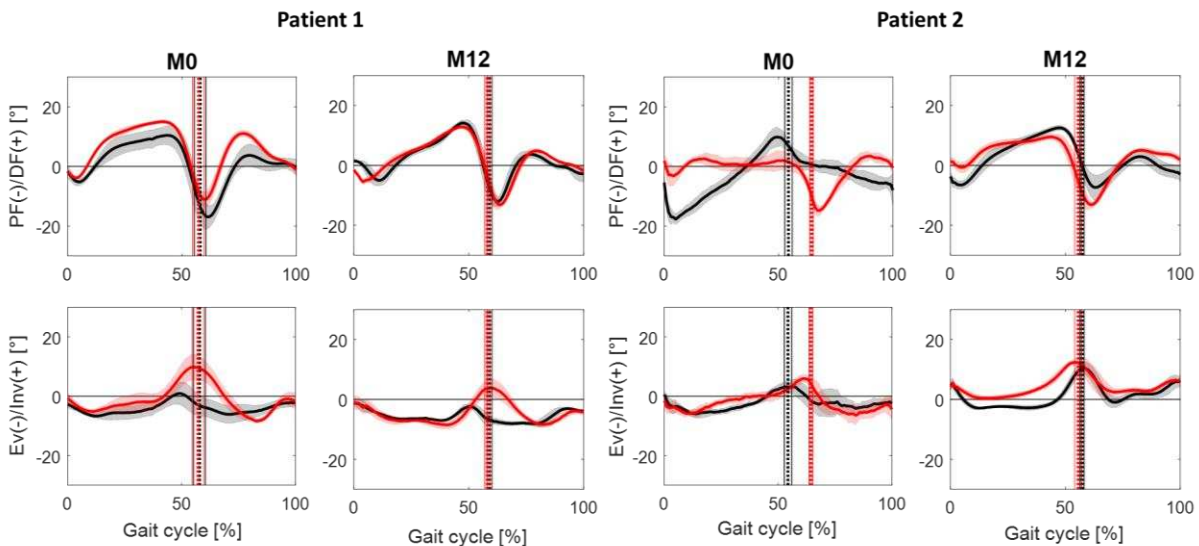
Angle	Isman and Inman, 1969 (n=46) mean (\pmSD) [°]	Inman, 1976 (n=104) mean (\pmSD) [°]	Van den Bogert, 1994 (n=14) mean (\pmSD) [°]	This study (n=38) mean (\pmSD) [°]
Gender	NA	NA	males	30 females/8 males
Age	Adults (age not specified)	Adults (age not specified)	Adults (age not specified)	11.2 \pm 3.1 years
<i>TibIncl</i>	80(\pm 4)	82.7(\pm 3.7) ($n=107$)	85.4(\pm 7.4)	90.7(\pm 4.1)
<i>TibDev</i>	84(\pm 7)	-	89.0(\pm 15.1)	82.7(\pm 7.4)
<i>SubIncl</i>	41(\pm 9)	42(\pm 9)	35.3(\pm 4.8)	41.1(\pm 14.1)
<i>SubDev</i>	23(\pm 11)	23(\pm 11)	18.0(\pm 16.2)	27.0(\pm 9.0)

257

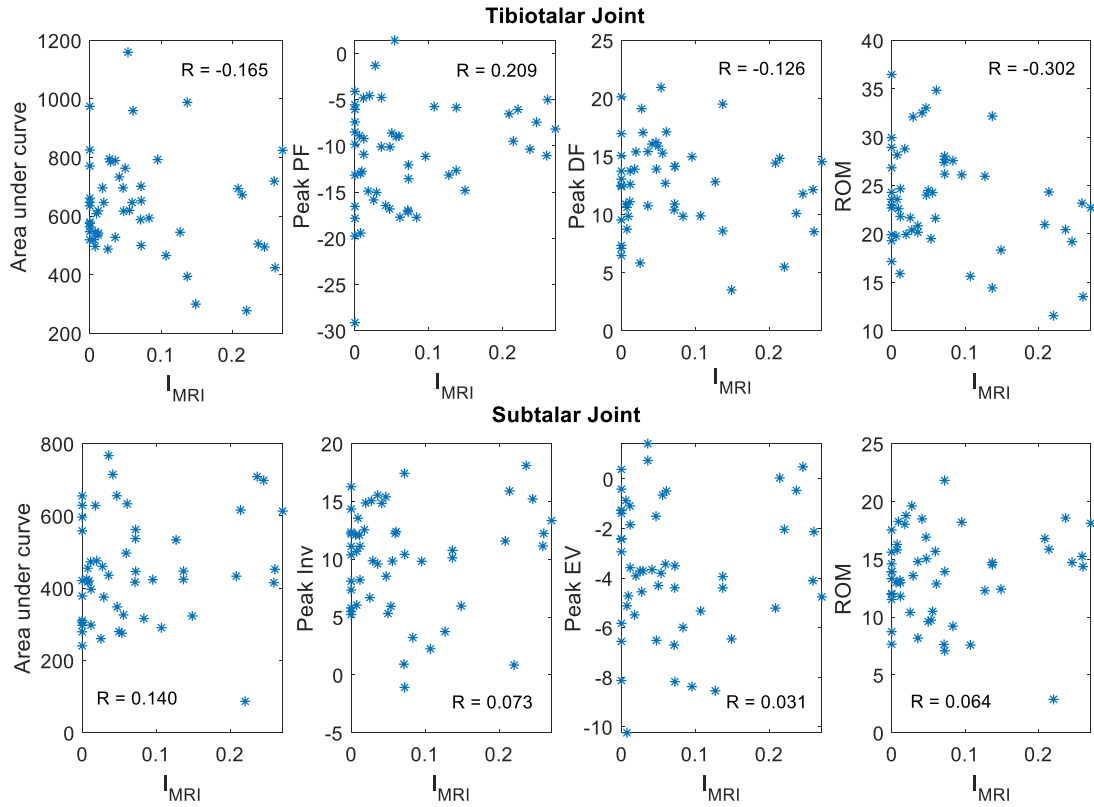
258 **Effect of clinical impairment on joint kinematics**

259 Figure 4 shows the estimated kinematics of two subjects with different clinical scoring: patient 1 was
260 similarly affected by the pathology at the two observations, whereas at M12 patient 2 was in total remission,
261 as defined by Ravelli and Martini (2007). This example highlights how the models clearly capture different
262 kinematic patterns associated with different paths of disease progression. The observation of the joint angles
263 also clearly indicates the ability of the model to describe changes in the gait patterns happening between
264 the two time-points, which were also confirmed by consistent changes in the walking speed (1.51 ± 0.05 m/s
265 at M0 and 1.22 ± 0.05 m/s at M12 for subject 1; 0.83 ± 0.03 m/s at M0 and 1.20 ± 0.04 m/s at M12 for subject
266 2). For the whole cohort, walking speed varied from 1.01 ± 0.24 m/s at M0 to 1.12 ± 0.13 m/s at M12, and was
267 1.14 ± 0.17 m/s and 0.93 ± 0.33 m/s at the “low-involvement” and “high-involvement” time-points
268 respectively, with no significant difference. Walking speed values did not correlate with the joint
269 impairment level, as measured with the I_{MRI} ($R = -0.21$ and $R = 0.16$ at M0 and M12, respectively). Similarly,
270 no correlation was observed between I_{MRI} and the kinematic parameters (Figure 5). This was confirmed by
271 the absence of a group-wise statistically significant difference between the joint kinematics of the ankles at
272 the “low-involvement” and “high-involvement” time-points throughout the gait cycle (Figure 6). Figure 7
273 clearly shows the absence of a significant correspondence between the asymmetry of impairment (ΔI_{MRI})
274 and the RMSD, MAV, ΔROM and ΔSD observed at M0 and M12. However, a smaller ΔI_{MRI} at M12 was

275 generally associated to a smaller value of the kinematics indices at that time-point, except for the Δ SD of
 276 the tibiotalar joint and the Δ ROM of the subtalar joint.



277 **Figure 4 - Tibiotalar (PF/DF) and subtalar (Ev/Inv) joints kinematics for two JIA patients at M0 and**
 278 **M12. Average right (left) kinematics is shown with black (red) solid line with shadow representing ± 1**
 279 **standard deviation. Toe off is shown with dotted vertical lines ± 1 standard deviation (solid vertical lines).**
 280 **Walking speed changed from 1.51 ± 0.05 m/s at M0 to 1.22 ± 0.05 m/s at M12 for patient 1 and from 0.83**
 281 **± 0.03 m/s at M0 and 1.20 ± 0.04 m/s at M12 for patient 2.**



282

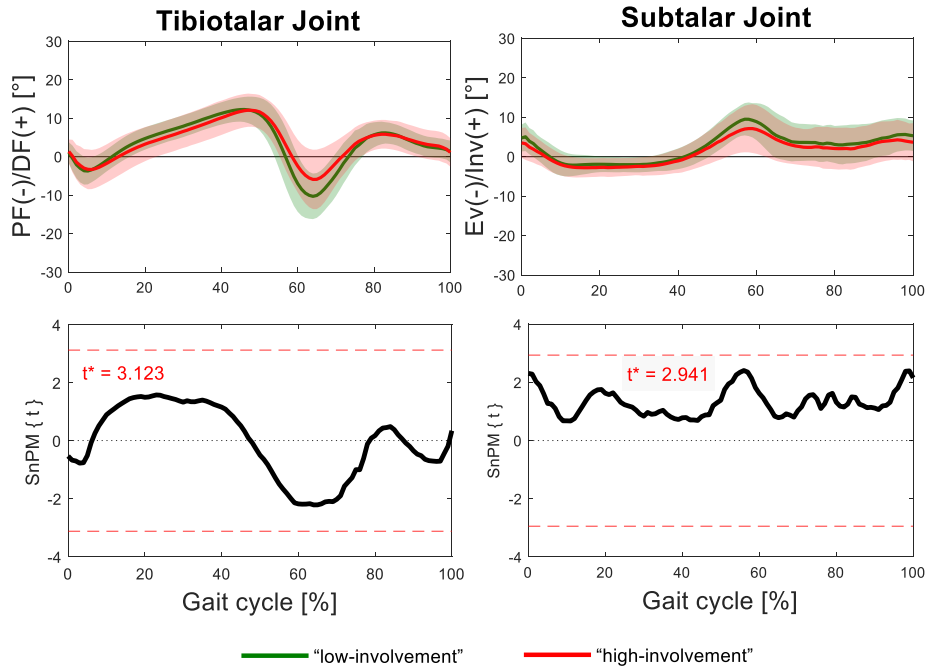
283 **Figure 5 - Correlation between joint impairment level (I_{MRI}) and joint kinematics parameters (area**
 284 **under the curve, peak of plantarflexion (Peak PF) and dorsiflexion (Peak DF), peak of Inversion (Peak**
 285 **Inv) and eversion (Peak Ev), ROM) for all feet and observations.**

286

287

288

289

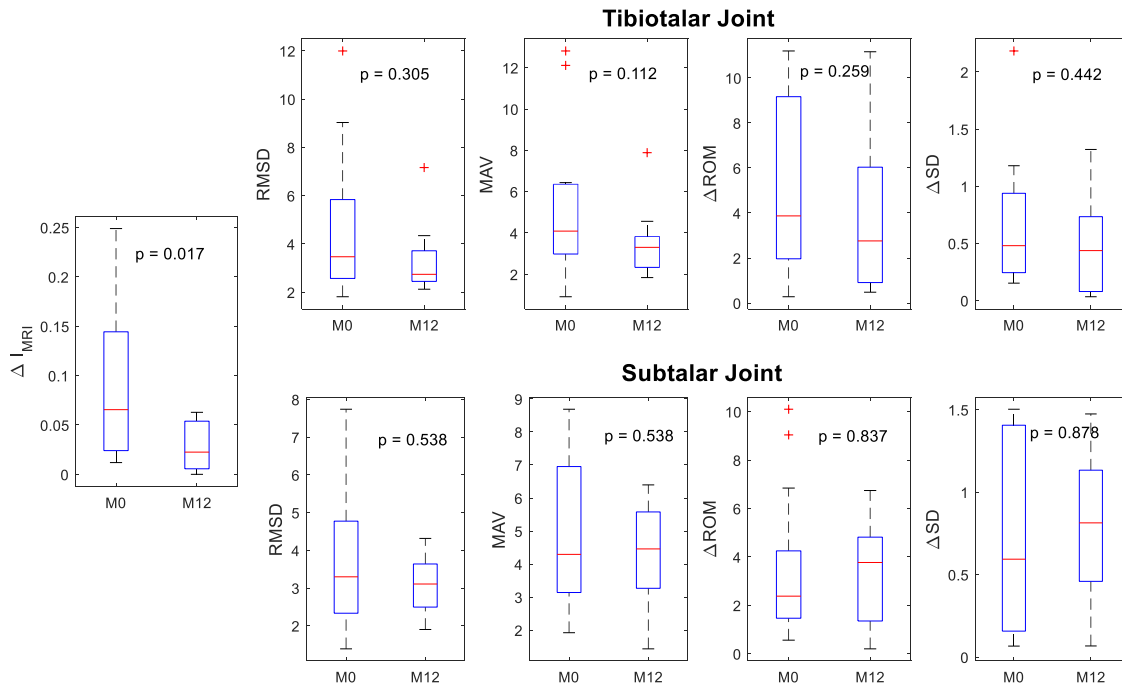


290

291 **Figure 6 - Tibiotalar (PF/DF) and subtalar (Ev/Inv) joint kinematics of the 13 subjects as calculated at**
 292 **the “low-involvement” (green) and “high-involvement” (red) time-point. Solid lines in the left graphs**
 293 **represent mean values and bands represent ± 1 standard deviation. The right figures show the**
 294 **corresponding distribution of t-values (SnPM{t}) throughout the gait cycle as obtained from the non-**
 295 **parametric 1D paired t-test (Nichols and Holmes, 2002), calculated using the SPM1D package (Pataky**
 296 **et al., 2012). Each group includes 24 mono-lateral models (2 models were excluded from the analysis).**

297

298



299

300 **Figure 7 – Boxplot distribution of ΔI_{MRI} and kinematics indices (RMSD, MAV, ΔROM and ΔSD) for**
 301 **both tibiotalar and subtalar joints (n=13) at M0 and M12. p-values from two-sided Wilcoxon signed-**
 302 **rank test are reported in each plot. Data outliers are marked with a +.**

303 Discussion

304 The aim of the study was to propose a kinematic model of the tibiotalar and subtalar joints, and to use this
 305 model to investigate the ankle joint kinematics in a group of children with JIA. The anatomical model was
 306 based on a morphological fitting approach and underwent repeatability analysis.

307 The procedure proved to be robust to the operator-dependent input. Even in the worst-case scenario, where
 308 the definition of the subtalar axis was associated with high inter-operator error (9.6°), the joint kinematics
 309 varied less than 1.3° . The inter-operator variability was mainly associated with the quality of the segmented
 310 images, i.e. low resolution, bias field or noise in the MRI, and to the complexity of segmenting bone tissue
 311 in young subjects, where cortical bone is not completely ossified (Evans, 2010). Nonetheless, this error was
 312 still acceptable when compared to other possible sources of variability coming from the experimental errors,
 313 such as instrumental error and marker placement error (up to $6^\circ \pm 2^\circ$ at the toe off (Di Marco et al., 2016)),

314 or soft tissue artefact (up to 20% of variability in the ankle kinematics (Lamberto et al., 2016)), confirming
315 the chosen morphological fitting approach is suitable in the presence of low quality images and/or poor
316 bone reconstructions.

317 An in vivo validation of the proposed technique was not possible within the framework of this project due
318 to ethics constraint in the use of approaches like dual-fluoroscopy in a paediatric population. However, the
319 comparison with ex vivo (Isman and Inman, 1969; Inman, 1976), and in vivo (Van den Bogert et al., 1994)
320 data certainly support the validity of the technique. Previous studies (Leitch et al., 2010; Van den Bogert et
321 al., 1994) reported the highest between-subject variabilities in the deviation angle (up to 15°); conversely,
322 we found the biggest differences in the inclination of the subtalar axis (14 °). This could be ascribed to the
323 subtalar axis' definition relying on the identification of the anterior facet of the talus. In the youngest
324 children, in fact, this surface can present a layer of unossified cartilage (Evans et al., 2010), which can
325 complicate the identification of the bone contour in the MRI, consequently affecting the results of
326 segmentation and morphological fitting.

327 The second goal of the study involved the application of the modelling approach as part of the clinical gait
328 assessment of patients with JIA. The between-session repeatability showed no statistically significant
329 difference between the measures of InterAxis at M0 and M12, confirming our hypothesis.

330 The observed joint kinematics reflected the heterogeneous and patient-specific nature of the pathology,
331 which presents several sub-types, each with a specific progression (Ravelli and Martini, 2007). In fact, the
332 individual differences (Figure 4) were not representative of a group behaviour (Figure 6) as a consequence
333 of different possible evolutions of the disease. The absence of a recognisable group pattern was
334 demonstrated by the lack of a direct relationship between a joint's clinical impairment and its kinematics.
335 The inter-subject variability was probably exacerbated by the heterogeneity of the cohort in terms of age,
336 anthropometry, disease subtype and activity level. This explains the lack of correlation between joint
337 kinematics (and their changes between time points) and the patient's I_{MRI} scores. This also held true for
338 the walking speed, which was not correlated with the MRI scores, but was found in line with the

339 1.17±0.02m/s reported by Esbjörnsson et al., 2015 for a group of JIA children with similar ankle
340 involvement. If group stratification needs to be pursued, then further investigation should aim at involving
341 larger subgroups for every sub-type of JIA and matching them by age and size.

342 The analysis of the between-limb asymmetry at the two time-points showed similar trends in the distribution
343 of ΔI_{MRI} and in the observed kinematics indices, despite none of the latter was significantly different
344 between the two time-points. In the tibiotalar articulation, lower ΔI_{MRI} at M12 corresponded to smaller
345 RMSD and MAV, confirming the asymmetry in the clinical involvement of the ankles is reflected by an
346 asymmetry in the biomechanics of gait. The subtalar kinematics was in general less informative and this is
347 probably associated to a smaller ROM of this joint when compared to the tibiotalar joint, potentially
348 resulting in smaller sensitivity to kinematics changes. Furthermore, disease-related alterations in the
349 movement are likely to be compensated by the tibiotalar joint being dominant in the ankle kinematics
350 (Lundberg et al., 1989) and therefore limiting the role of the subtalar joint. The lack of an independent
351 clinical assessment of the two joints must be considered as a limitation in the study. In fact, the present
352 work is based on the assumption that the I_{MRI} score, evaluating the overall condition of the ankle joint, is
353 representative of both tibiotalar and subtalar impairment level. Nonetheless, a different level of involvement
354 of the two joints could justify their different biomechanical response. Lastly, the assumption made in
355 schematising the joints as hinge-like mechanisms represents a substantial simplification of the true
356 articulating surfaces, potentially limiting the representation of their true 3D motion. However, the tibiotalar
357 kinematics was only marginally affected by this modelling choice, as this movement mainly occurs in the
358 sagittal plane (Roach et al., 2016). On the contrary, the subtalar joint might benefit from a more detailed
359 representation and further studies are needed to investigate this aspect.

360 In conclusion, this study showed the feasibility of using morphological fitting of MRI-based bone
361 segmentation to identify the tibiotalar and subtalar joint axes in a non-invasive patient-specific manner.
362 Including these joints in a musculoskeletal model of the lower limb, coupled with an appropriate marker
363 set, can give a better understanding of their individual contribution to the ankle biomechanics. This supports

364 the adoption of the proposed modelling procedure into the practice of lower limb musculoskeletal modelling
365 for the quantification of ankle biomechanics. The application to a pathological population, children with
366 JIA, unveiled for the first time the absence of correlation between ankle impairment and biomechanical
367 function, confirming the heterogeneous and systemic nature of this disease.

368 **Conflict of interest**

369 The authors declare they do not have any financial or personal relationships with other people or
370 organizations that could have inappropriately influenced this study.

371 **Acknowledgments**

372 The authors want to acknowledge Dr Norman Powell for the writing assistance. This research was
373 supported by the European Commission (MD-PAEDIGREE project, FP7-ICT Programme, Project ID:
374 600932) and by the UK EPSRC (Multisim project, Grant number: EP/K03877X/1).

375 **References**

- 376 Arndt, A., Westblad, P., Winson, I., Hashimoto, T., Lundberg, A., 2004. Ankle and Subtalar Kinematics
377 Measured with Intracortical Pins During the Stance Phase of Walking. *Foot Ankle Int.* 25, 357-364.
- 378 Arndt, A., Wolf, P., Nester, C., Liu, A., Jones, R., Howard, D., Stacoff, A., Lundgren, P., Lundberg, A.,
379 2006. Intrinsic foot motion measured in vivo during barefoot running. *Journal of Biomechanics* 39, S182-
380 S182.
- 381 Baker, R., 2003. Letter to the editor: ISB recommendation on definition of joint coordinate systems for the
382 reporting of human joint motion—part I: ankle, hip and spine. *Journal of Biomechanics* 36(2), 300-302
- 383 Bartlett, R., 2007. Introduction to sports biomechanics: analysing human movement patterns (2nd Ed.).
384 Routledge, Abingdon, England
- 385 Barnett, G.H. and Napier, J.R., 1952. The Axis of Rotation at the Ankle Joint in Man. Its Influence upon
386 the Form of the Talus and the Mobility of the Fibula. *J. Anat. Lond.*, 86: 1-9.
- 387 Cignoni, P., Callieri, M., Corsini, M., Dellepiane, M., Ganovelli, F. and Ranzuglia, G., 2008. Meshlab: an
388 open-source mesh processing tool. Eurographics Italian Chapter Conference.
- 389 Correa, T.A., Pandy, M.G., 2011. A mass-length scaling law for modelling muscle strength in the lower
390 limb. *Journal of Biomechanics* 44 (16), 2782-2789

391 Delp, S.L., Loan, J.P., Hoy, M.G., Zajac, F.E., Topp, E.L. and Rosen, J.M., 1990. An interactive graphics-
392 based model of the lower extremity to study orthopaedic surgical procedures. *IEEE Transactions on*
393 *Biomedical Engineering* 37, 757-767.

394 Delp, S. L., Anderson, F. C., Arnold, A. S., Loan, P., Habib, A., John, C. T., Guendelman, E. and Thelen,
395 D. G., 2007. OpenSim: open-source software to create and analyze dynamic simulations of movement.
396 *IEEE Transactions on Biomedical Engineering* 54, 1940-1950.

397 Dettwylera, M., Stacoffa, A., Kramers-de Quervaina, I.A., Stüssia, E., 2004. Modelling of the ankle joint
398 complex. Reflections with regards to ankle prostheses. *Foot Ankle Surg.* 10, 109–119.

399 Di Marco, R., Rossi, S., Racic V., Cappa, P., Mazzà, C., 2016. Concurrent repeatability and reproducibility
400 analyses of four marker placement protocols for the foot-ankle complex. *Journal of Biomechanics* 49,
401 3168–3176.

402 Di Marco, R., Scalona, E., Pacilli, A., Cappa, P., Mazzà, C., Rossi, S., 2018. How to choose and interpret
403 similarity indices to quantify the variability in gait joint kinematics. *International Biomechanics* 5(1), 1–8

404 Dul, J., Johnson, G.E., 1985. A kinematic model of the ankle joint. *J Biomed Eng.* 7, 137-143.

405 Durkin, J.L., Dowling, J.J., 2006. Body Segment Parameter Estimation of the Human Lower Leg Using an
406 Elliptical Model with Validation from DEXA. *Annals of Biomedical Engineering* 34, 1483–1493.

407 Evans, A., 2010. *Paediatrics. The Pocket Podiatry Guide.* Churchill Livingstone Elsevier.

408 Esbjörnsson, A. C., Iversen, M. D., André, M., Hagelberg, S., Schwartz, M. H., & Broström, E. W. (2015).
409 Effect of intraarticular corticosteroid foot injections on walking function in children with juvenile idiopathic
410 arthritis. *Arthritis care & research*, 67(12), 1693-1701.

411 Fick, R., 1911. *Handbuch der Anatomie und Mechanik der Gelenke: III, Spezielle Gelenk-und*
412 *Muskelmechanik*, Gustav Fischer Verlag, Jena

413 Hannah, I., Montefiori, E., Modenese, L., Prinold, J., Viceconti, M. and Mazzà, C., 2017. Sensitivity of a
414 juvenile subject-specific musculoskeletal model of the ankle joint to the variability of operator-dependent
415 input. *Proceedings of the Institution of Mechanical Engineers, Part H: Journal of Engineering in Medicine*
416 231, 415-422.

417 Hicks, J.H., 1953. The mechanics of the foot: the joints. *Journal of Anatomy* 87, 345-357

418 Hicks, J., Uchida, T., Seth, A., Rajagopal, A. and Delp, S. L., 2015. Is my model good enough? Best
419 practices for verification and validation of musculoskeletal models and simulations of human movement.
420 *Journal of Biomechanical Engineering* 137(2):020905.

421 Inman, V.T., 1976. *The Joints of the Ankle.* Williams and Wilkins, Baltimore.

422 Isman, R. E. and Inman, V. T., 1968. Anthropometric studies of the human foot and ankle. *Bulletin of*
423 *prosthetics research* 10/11, 97-129.

424 Lamberto, G., Martelli, S., Cappozzo, A., Mazzà, C., 2017. To what extent is joint and muscle mechanics
425 predicted by musculoskeletal models sensitive to soft tissue artefacts? *Journal of Biomechanics* 62, 68-

426 76.Leitch, J., Stebbins, J., Zavatsky, A.B., 2010. Subject-specific axes of the ankle joint complex. *Journal of Biomechanics* 43, 2923–2928
427

428 Leitch, J., Stebbins, J., Zavatsky, A.B., 2010. Subject-specific axes of the ankle joint complex. *Journal of*
429 *Biomechanics* 43, 2923–2928

430 Lewis, G.S., Cohen, T.L., Seisler, A.R., Kirby, K.A., Sheehan, F.T., Piazza, S.J., 2009. In vivo tests of an
431 improved method for functional location of the subtalar joint axis. *Journal of Biomechanics* 42, 146–151.

432 Lundberg, A., 1989. Kinematics of the ankle and foot: in vivo roentgen stereophotogrammetry. Ph.D.
433 Thesis, Department of Orthopaedics, Karolinska Hospital, Stockholm, Sweden. *Acta Orthopaedica*
434 *Scandinavia* 60 (Suppl.), 233.

435 Manter, J.T., 1941. Movements of the subtalar and transverse tarsal joints. *The Anatomical Record* 80, 397.

436 Malaquias, T.M., Silveira, C., Aerts, W., De Groote, F., Dereymaeker, G., Vander Sloten, J., Jonkers, I.,
437 2017. Extended foot-ankle musculoskeletal models for application in movement analysis. *Computer*
438 *Methods in Biomechanics and Biomedical Engineering* 20:2, 153-159

439 Malattia, C., Damasio, M.B., Pistorio, A., Ioseliani, M., Vilca, I., Valle, M., Ruperto, N., Viola, S.,
440 Buoncompagni, A., Magnano, G.M., Ravelli, A., Tomà, P., Martini, A., 2011. Development and
441 preliminary validation of a paediatric-targeted MRI scoring system for the assessment of disease activity
442 and damage in juvenile idiopathic arthritis. *Annals of the Rheumatic Diseases* 70, 440-6.

443 Mattingly, B., Talwalkar, V., Tylkowski, C., Stevens, D.B., Hardy, P.A., Pienkowski, D., 2006. Three-
444 dimensional in vivo motion of adult hind foot bones. *Journal of Biomechanics* 39 (4), 726-733.

445 Modenese, L., Montefiori, E., Wang, A., Wesarg, S., Viceconti, M., Mazzà, C., 2018. Investigation of the
446 dependence of joint contact forces on musculotendon parameters using a codified workflow for image-
447 based modelling. *Journal of Biomechanics* 73, 108-118.

448 Nichols, T.E., Holmes, A.P., 2002. Nonparametric permutation tests for functional neuroimaging: a primer
449 with examples. *Human Brain Mapping* 15(1), 1–25.

450 Nusman, C.M., Ording Muller, L.S., Hemke, R., Doria, A.S., Avenarius, D., Tzaribachev, N., et al., 2016.
451 Current Status of Efforts on Standardizing Magnetic Resonance Imaging of Juvenile Idiopathic Arthritis:
452 Report from the OMERACT MRI in JIA Working Group and Health-e-Child. *The Journal of*
453 *Rheumatology* 43:239-244.

454 Ostergaard, M., Peterfy, C., Conaghan, P., McQueen, F., Bird, P., Ejbjerg, B., et al., 2003. OMERACT
455 Rheumatoid Arthritis Magnetic Resonance Imaging Studies. Core set of MRI acquisitions, joint pathology
456 definitions, and the OMERACT RA-MRI scoring system. *The Journal of Rheumatology* 30:1385-6.Parr,
457 W. C. H., Chatterjee, H. J. and Soligo, C., 2012. Calculating the axes of rotation for the subtalar and
458 talocrural joint using 3D bone reconstructions. *Journal of Biomechanics* 45, 1103-1107.

459 Parr, W. C. H., Chatterjee, H. J. and Soligo, C., 2012. Calculating the axes of rotation for the subtalar and
460 talocrural joint using 3D bone reconstructions. *Journal of Biomechanics* 45, 1103-1107.

461 Pataky, T.C., 2012. One-dimensional statistical parametric mapping in Python. *Comput. Methods Biomech.*
462 *Biomed. Eng.* 15, 295–301

463 Prinold, J. I., Mazzà, C., Di Marco, R., Hannah, I., Malattia, C., Magni-Manzoni, S., Petrarca, M.,
464 Ronchetti, A., Tanturri de Horatio, L., van Dijkhuizen, E. H. P., Wesarg, S. and Viceconti, M., 2016. A
465 Patient-Specific Foot Model for the Estimate of Ankle Joint Forces in Patients with Juvenile Idiopathic
466 Arthritis. *Annals of biomedical engineering* 44, 247-257.

467 Rasmussen, O., Tovborg-Jensen, I., 1982. Mobility of the ankle joint: recording of rotator movements in
468 the talocrural joint in vitro with and without the lateral collateral ligaments of the ankle. *Acta Orthop Scand*
469 53, 155–60.

470 Ravelli A. and Martini A., 2007. Juvenile idiopathic arthritis. *Lancet* 369(9563), 767-778.

471 Roaas, A., Anderson, G.B., 1982. Normal range of motion of the hip, knee and ankle joints in male subjects,
472 30-40 years of age. *Acta Orthop Scand* 53(2), 205-8.

473 Roach, K.E., Wang, B., Kapron, A.L., Fiorentino, N.M., Saltzman, C.L., Foreman, K.B., Anderson, A.E.
474 In Vivo Kinematics of the Tibiotalar and Subtalar Joints in Asymptomatic Subjects: A High-Speed Dual
475 Fluoroscopy Study. *ASME. J Biomech Eng.* 2016;138(9):091006-091006-9.

476 Saraswat, P., Andersen, M.S., MacWilliams, B.A., 2010. A musculoskeletal foot model for clinical gait
477 analysis. *Journal of Biomechanics* 43 (9), 1645-1652.

478 Scheys, L., Loeckx, D., Spaepen, A., Suetens, P. and Jonkers, I., 2009. Atlas-based non-rigid image
479 registration to automatically define line-of-action muscle models: A validation study. *Journal of*
480 *Biomechanics* 42, 565-572.

481 Scott, S.H., Winter, D.A., 1991. Talocrural and talocalcaneal joint kinematics and kinetics during the stance
482 phase of walking. *J. Biomech.* 24, 743–752.

483 Sepic, S. B., Murray, M. P., Mollinger, L. A., Spurr, G. B., & Gardner, G. M. 1986. Strength and range of
484 motion in the ankle in two age groups of men and women. *American Journal of Physical Medicine* 65, 75-
485 84.

486 Siegler, S., Chen, J., Schneck, C.D., 1988. The three-dimensional kinematics and flexibility characteristics
487 of the human ankle and subtalar joints. Part 1: kinematics. *Journal of Biomechanical Engineering* 110, 364–
488 373.

489 Siegler, S., Toy, J., Seale, D., & Pedowitz, D. (2014). The clinical biomechanics award 2013 - presented
490 by the international society of biomechanics: New observations on the morphology of the talar dome and
491 its relationship to ankle kinematics. *Clinical Biomechanics*, 29(1), 1-6.

492 Stebbins, J., Harrington, M., Thompson, N., Zavatsky, A. and Theologis, T., 2006. Repeatability of a model
493 for measuring multi-segment foot kinematics in children. *Gait & Posture* 23, 401-410.

494 Steger, S., Kirschner, M. and Wesarg, S., 2012. Articulated atlas for segmentation of the skeleton from
495 head & neck CT datasets. 9th IEEE International Symposium on Biomedical Imaging (ISBI). Barcelona,
496 Spain.

497 Valente, G., Crimi, G., Vanella, N., Schileo, E. and Taddei, F., 2017. nmsBuilder: Freeware to create
498 subject-specific musculoskeletal models for OpenSim. *Computer Methods and Programs in Biomedicine*
499 152, 85-92.

500 van den Bogert, A.J., Smith, G.D., Nigg, B.M., 1994. In vivo determination of the anatomical axes of the
501 ankle joint complex: an optimization approach. *Journal of Biomechanics* 27, 1477–1488

502 van Langelaan, E.J., 1983. A kinematical analysis of the tarsal joints. An X-ray photogram-metric study.
503 Ph.D. Thesis, *Acta Orthopaedica Scandinavia* 54 (Suppl.), 204.

504 Vicon Motion Systems, L. Biomechanical Research, 2012. [http://www.irc-
506 web.co.jp/vicon_web/news_bn/PIGManualver1.pdf](http://www.irc-
505 web.co.jp/vicon_web/news_bn/PIGManualver1.pdf)

507 Westblad, P., Hashimoto, T., Winson, I., Lundberg, A., Arndt, A., 2002. Differences in ankle-joint complex
508 motion during the stance phase of walking as measured by superficial and bone-anchored markers. *Foot
509 Ankle Int.* 23 (9), 856–863.

510 Woltring, H.J., 1986. A FORTAN package for generalized cross-validatory spline smoothing and
511 differentiation. *Advances in Engineering Software* 8(2), 104-113.

512